EMBO reports

scientific report

Mutation in the *Scyl1* gene encoding amino-terminal kinase-like protein causes a recessive form of spinocerebellar neurodegeneration

Wolfgang M. Schmidt [1,2], Cornelia Kraus [3], Harald Höger [4], Sonja Hochmeister [5], Felicitas Oberndorfer [1], Manuela Branka [1], Sonja Bingemann [1], Hans Lassmann [5], Markus Müller [2], Lúcia Inês Macedo-Souza [6], Mariz Vainzof [6], Mayana Zatz [6], André Reis [3] & Reginald E. Bittner [1+]

[1]Neuromuscular Research Department, Center of Anatomy & Cell Biology, Medical University of Vienna, Vienna, Austria, [2]Department of Clinical Pharmacology, Section of Cardiovascular Medicine, Medical University of Vienna, Vienna, Austria, [3]Institute of Human Genetics, Friedrich-Alexander-University Erlangen-Nuremberg, Erlangen, Germany, [4]Division for Laboratory Animal Science and Genetics, Medical University of Vienna, Himberg, Austria, [5]Center for Brain Research, Division of Neuroimmunology, Medical University of Vienna, Vienna, Austria, and [6]Department of Biology, Institute of Biological Sciences and Center for Study of Human Genome, University of São Paulo, São Paulo, Brazil

Here, we show that the murine neurodegenerative disease *mdf* (autosomal recessive mouse mutant 'muscle deficient') is caused by a loss-of-function mutation in *Scyl1*, disrupting the expression of N-terminal kinase-like protein, an evolutionarily conserved putative component of the nucleocytoplasmic transport machinery. Scyl1 is prominently expressed in neurons, and enriched at central nervous system synapses and neuromuscular junctions. We show that the pathology of *mdf* comprises cerebellar atrophy, Purkinje cell loss and optic nerve atrophy, and therefore defines a new animal model for neurodegenerative diseases with cerebellar involvement in humans.

Keywords: muscle deficient (*mdf*); motor neuron disease Purkinje cells; SCY1-like 1 (S. cerevisiae); spinocerebellar ataxia

EMBO reports (2007) **8**, 691–697. doi:10.1038/sj.embor.7401001

[1]Neuromuscular Research Department, Center of Anatomy & Cell Biology, Medical University of Vienna, Währinger Strasse 13, A-1090 Vienna, Austria
[2]Department of Clinical Pharmacology, Section of Cardiovascular Medicine, Medical University of Vienna, Währinger Gürtel 18-20, A-1090 Vienna, Austria
[3]Institute of Human Genetics, Friedrich-Alexander-University Erlangen-Nuremberg, Schwabachanlage 10, D-91054 Erlangen, Germany
[4]Division for Laboratory Animal Science and Genetics, Medical University of Vienna, Brauhausgasse 34, A-2325 Himberg, Austria
[5]Center for Brain Research, Division of Neuroimmunology, Medical University of Vienna, Spitalgasse 4, A-1090 Vienna, Austria
[6]Department of Biology, Institute of Biological Sciences and Center for Study of Human Genome, University of São Paulo, Rua do Matão, 277 Cidade Universitária, São Paulo, Brazil
[+]Corresponding author. Tel: +43 664 80016 37514; Fax: +43 1 4277 61198; E-mail: reginald.bittner@meduniwien.ac.at

Received 23 February 2007; revised 30 April 2007; accepted 30 April 2007; published online 15 June 2007

INTRODUCTION

So far, several molecular mechanisms associated with specific neurodegenerative disorders have been identified; however, a vast majority of diseases characterized by neuronal degeneration and the resultant disabilities such as muscular atrophy, motor dysfunction and paralysis are still poorly understood. Most of these diseases are fatal and no therapeutic strategies are available. Therefore, identification of new molecules involved in cellular pathways, which are indispensable for neuronal and neuromuscular functional integrity and that could be targeted therapeutically is crucial.

To this end, we investigated the molecular defect underlying the autosomal recessive mouse mutant 'muscle deficient' (*mdf*; Womack *et al*, 1980; Sweet, 1983). Although several clinical and pathological changes such as progressive neuromuscular atrophy and hindlimb paralysis are compatible with motor neuron disease (Blot *et al*, 1995), the *mdf* mouse also shows phenotypes indicating cerebellar involvement such as gait ataxia, abnormal hindlimb posture and tremor (supplementary Fig 1 and video 1 online). Therefore, we proposed that *mdf* can be linked to both motor neuron disease and spinocerebellar ataxia (SCA), thus representing an important model for recessively inherited neurodegenerative disorders in humans.

RESULTS AND DISCUSSION

By using intercross breeding strategies, we confined the *mdf* locus that had been previously mapped to mouse chromosome 19 A (Sweet, 1983; Poirier *et al*, 1998). Among the 48 candidate genes within the approximately 0.9 Mb *mdf* region, we identified *Scyl1* (*RefSeq* DNA NM_023912.1) as the disease causing gene after we detected an inserted thymidine in exon 8 (Fig 1A). This mutation

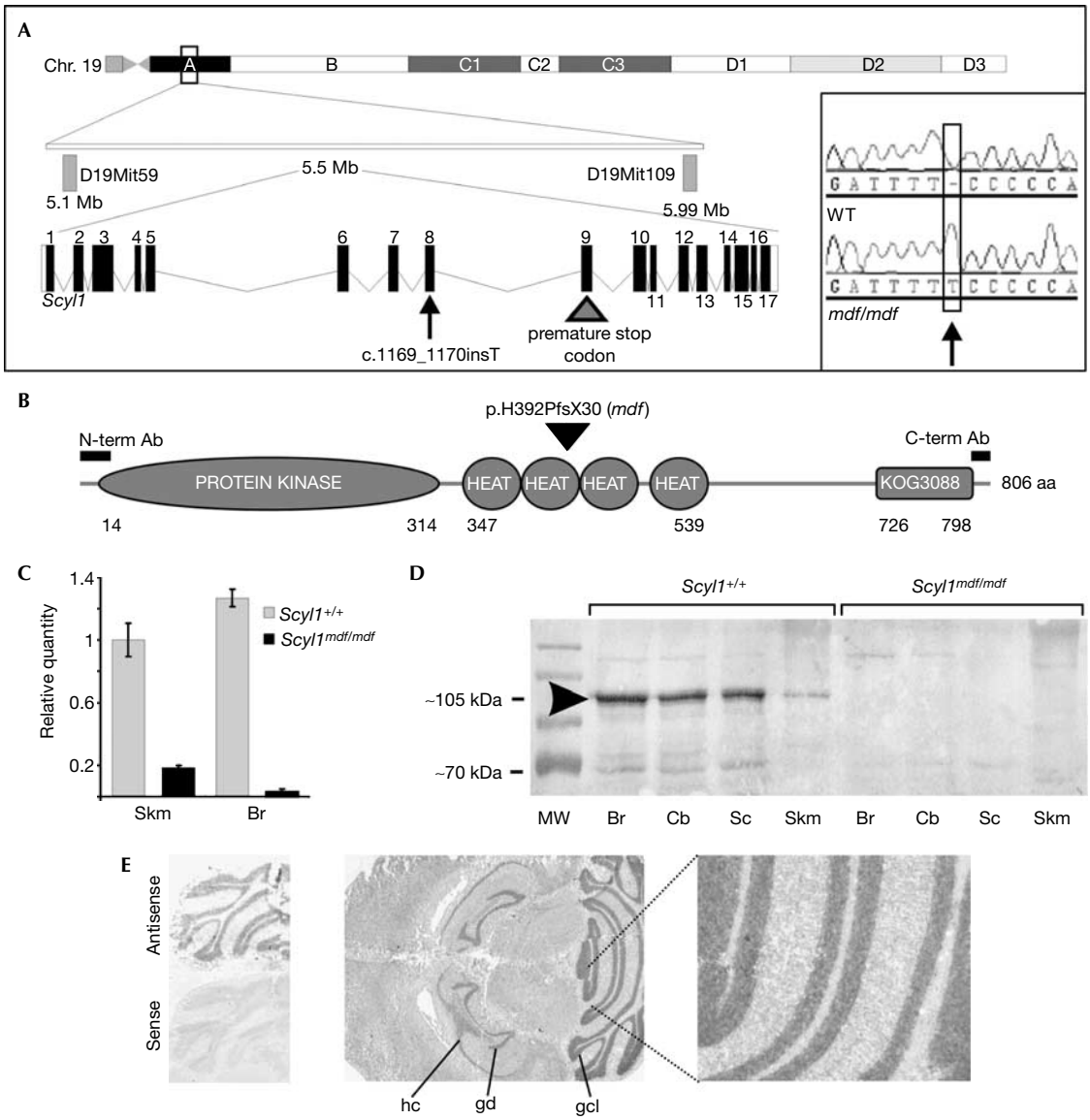

Fig 1 | A single thymidine-nucleotide insertion causes disruption of Scyl1 expression in the *mdf*–mouse. (**A**) Mapping of sequence tagged sites located *mdf* to an approximately 0.9 Mb chromosomal region between D19Mit59 and D19Mit109. Location of *Scyl1* is indicated and the exon–intron structure depicted (the exons are numbered). The *mdf* mutation is indicated by an arrow (inset: representative sequence traces showing the nucleotide insertion at position c.1169_1170insT). (**B**) Schematic '*in silico*' annotation of Scyl1 protein domains (numbers indicate amino-acid (aa) residues): serine–threonine-tyrosine protein kinase, HEAT repeats, secretory carrier membrane protein domain (KOG3088). Positions of peptides for raising antibodies (Ab) are shown. The premature stop codon created by the *mdf* mutation is indicated (arrowhead). (**C**) Quantitative reverse transcription–PCR of total RNA isolated from skeletal muscle (Skm) or brain (Br) showing a marked reduction of *Scyl1* messenger RNA in $Scyl1^{mdf/mdf}$. Error bars indicate standard deviation ($n = 4$). (**D**) Western blot loaded with extracts from brain (Br), cerebellum (Cb), spinal cord (Sc) and skeletal muscle (Skm) of wild-type $Scyl1^{+/+}$ and $Scyl1^{mdf/mdf}$ mice probed with polyclonal antibody raised against the amino terminus of Scyl1. In wild-type tissues, the antibody detected an approximately 105 kDa band (arrowhead) that was completely absent in corresponding tissues from $Scyl1^{mdf/mdf}$ mice. A second, minor reactive band of approximately 70 kDa is also indicated. MW, molecular weight standard (~70, ~100, ~130, ~150 kDa). (**E**) Detection of *Scyl1*-mRNA by *in situ* hybridization (ISH) in a wild-type mouse brain section showing high expression in the granular and Purkinje cell layers of the cerebellum (gcl), the hippocampus (hc) and the gyrus dentatus (gd). Right panel is a magnified view showing abundant *Scyl1* expression in the synaptic region of the cerebellar granular layer. Left panel: control experiments showing specificity of the antisense ISH probe as opposed to the sense control probe.

fully segregated with the disease phenotype on different genetic backgrounds (supplementary video 2 online) and all parental breeders, as well as approximately 50% of their offspring, were heterozygous carriers. We also found the mutation in an *mdf/mdf* DNA sample obtained directly from the Jackson Laboratories (Bar Harbor, ME, USA), where the mutant originally arose (Womack

et al, 1980). We suggest renaming this spontaneous mouse mutant *Scyl1*^{mdf}. As the insertion within *Scyl1* exon 8 (c.1169_1170insT) causes a frame shift and creates a premature stop codon (p.H392PfsX30), we wanted to confirm the predictably deleterious consequences for messenger RNA and protein expression, respectively. By using quantitative mRNA assays, we found that *Scyl1* transcripts were markedly reduced in nervous tissues and to a lesser extent in skeletal muscle from *Scyl1*$^{mdf/mdf}$ mice, which is indicative of nonsense-mediated mRNA decay (Fig 1C).

Scyl1 is highly conserved among eukaryotes and contains an amino-terminal serine–threonine kinase-like domain (Liu *et al*, 2000; Kato *et al*, 2002). Further domains, detected by *in silico* annotation, comprise four HEAT repeats and a secretory carrier membrane protein domain (Fig 1B), indicating that Scyl1 interacts with other proteins and is involved in intracellular transport processes. To investigate Scyl1 expression and distribution, we raised antibodies against N- and carboxy-terminal peptides. On western blots, both antibodies detected a major immunoreactive band with a molecular weight of approximately 105 kDa, which is in accordance with previously reported migration properties (Liu *et al*, 2000), in all probed murine and human tissue extracts. By contrast, the antibodies failed to detect a corresponding band in all tissue extracts from mutant *Scyl1*$^{mdf/mdf}$ mice, indicating that the mutation causes a complete loss of full-length Scyl1 protein (supplementary Fig 2A online). No lower-molecular-weight bands were detected by the antibody against the N terminus in *Scyl1*$^{mdf/mdf}$ tissues, indicating the absence of truncated protein products (Fig 1D). When we probed brain sections using *in situ* hybridization, we found prominent *Scyl1* expression confined to the neuronal perikarya—most pronounced in the Purkinje cells in the cerebella of normal mice (Fig 1E)—which is fully compatible with expression patterns shown in the Allen Brain Atlas (Lein *et al*, 2007). Scyl1-specific antibodies intensely labelled all central nervous system (CNS) neurons in sections from wild-type mice and humans, whereas no such staining was observed in mutant *Scyl1*$^{mdf/mdf}$ CNS tissues (Fig 2A,B). We found prominent Scyl1 expression in all CNS neurons, including cortical neurons (Fig 2C), brain-stem neurons (Fig 2D) and anterior horn spinal cord motor neurons (Fig 2E).

In addition to Scyl1 expression throughout CNS neurons and neuronal dendrites (Fig 2C–F), the protein was also detected in the axons of peripheral nerves (Fig 2H), indicating axonal transport of Scyl1. In agreement with this hypothesis, we detected Scyl1 accumulation in axonal spheroids (Fig 2G): these age-related, neuropathological structures represent sites where axonally transported proteins usually accumulate. Furthermore, we found Scyl1 to be enriched at synapses in the CNS and in the periphery at the neuromuscular junction (Fig 2I), indicating further that Scyl1 is subjected to axonal transport.

As we detected prominent Scyl1 expression in Purkinje cells of the cerebella of wild-type mice and humans (Fig 3A,B), we investigated this cell type more closely in Scyl1-deficient mice and found that many Purkinje cells showed various pathological changes indicative of neuronal degeneration in *mdf* cerebella (Fig 3C). Our observation of basket formations devoid of Purkinje cells ('empty baskets'; inset in Fig 3C) indicates that pre-existing Purkinje cells have disappeared in Scyl1-deficient cerebella. Consistent with this observation, we found that the overall number of Purkinje cells in all areas of *Scyl1*$^{mdf/mdf}$ cerebella was markedly reduced (Fig 3D). As this reduction in Purkinje cells was already pronounced in young mutants (45 days), we propose that loss of Purkinje cells represents an early, pre-clinical pathology in *Scyl1*-deficient mice. Purkinje cell-related pathologies ranging from loss of Purkinje cells to multiple degenerative abnormalities became most clearly visible with Purkinje-cell-specific Calbindin staining (Fig 3E,F). Dendritic arborization of Purkinje cells was found to be markedly reduced—characterized by paucity of ramification and axonal swellings (inset in Fig 3F)—which is compatible with ongoing neurodegeneration. Whole median sagittal cross-sections showed a marked atrophy of the cerebellar vermis in *mdf* mice (Fig 3G,H).

Our findings on the cerebellar neuropathology in Scyl1-deficient mice suggest that the loss of Purkinje cells in *mdf* is an early-onset and progressive degenerative condition associated with atrophy rather than a developmental defect in the formation of the Purkinje cell layer. We have therefore unraveled a series of clinical and pathological findings in *mdf*, which are characteristic of SCA in humans and corresponding mouse models. This prompted us to investigate the optic nerve of *mdf* animals more closely, because optic atrophy represents a pathology common to several types of SCAs. Indeed, we found that *Scyl1*$^{mdf/mdf}$ optic nerve cross-sections from comparable retrobulbar regions had visibly smaller diameters when compared with wild-type samples (supplementary Fig 3A online). Morphometric analysis based on electron micrographs of ultrathin cross-sections from optic nerves showed a significantly increased proportion of small-diameter myelinated fibres and thinner myelin sheaths in 2-year-old *Scyl1*$^{mdf/mdf}$ mice compared with wild-type animals, compatible with hypomyelination and axonal degeneration (supplementary Fig 3B online). Recently, an autosomal recessive disorder, characterized by spastic paraplegia, optic atrophy and neuropathy (SPOAN), has been mapped to human chromosome 11q13, a region encompassing the human Scyl1 orthologue (Macedo-Souza *et al*, 2005). To test whether SPOAN represents the human *mdf* disease counterpart, we sequenced the entire *SCYL1* gene of two representative patients of two SPOAN families. However, we did not find any mutation, excluding SPOAN as the human disease counterpart.

In our study, Scyl1 emerged as a new protein essential for neuronal and, particularly, Purkinje cell survival, the disruption of which causes an early-onset and progressive neurodegenerative disorder. Intriguingly, recent evidence from a protein–protein interactome for human inherited diseases characterized by degeneration of Purkinje cells, developed by Lim *et al* (2006), readily supports the relevance of Scyl1 in the context of human neurodegenerative disorders: the human *SCYL1*-encoded protein was found to interact with the Coilin protein (COIL), which is also a binding partner for ataxin 1 (which causes SCA1), puratrophin 1 (implicated in degeneration of Purkinje cells) and Survival motor neuron protein (SMN; the loss of which causes spinal muscular atrophy). This established SCYL1 as a member of the 'ataxia-ome'—the protein–protein interaction network for human ataxias and disorders of Purkinje cell degeneration (Humbert & Saudou, 2006; Lim *et al*, 2006). Together with our findings, this classifies *SCYL1* as a putative candidate gene for human neurodegenerative diseases involving the cerebellum.

As for many proteins associated with disease, the precise cellular function of Scyl1 and its role in pathogenesis of neuronal

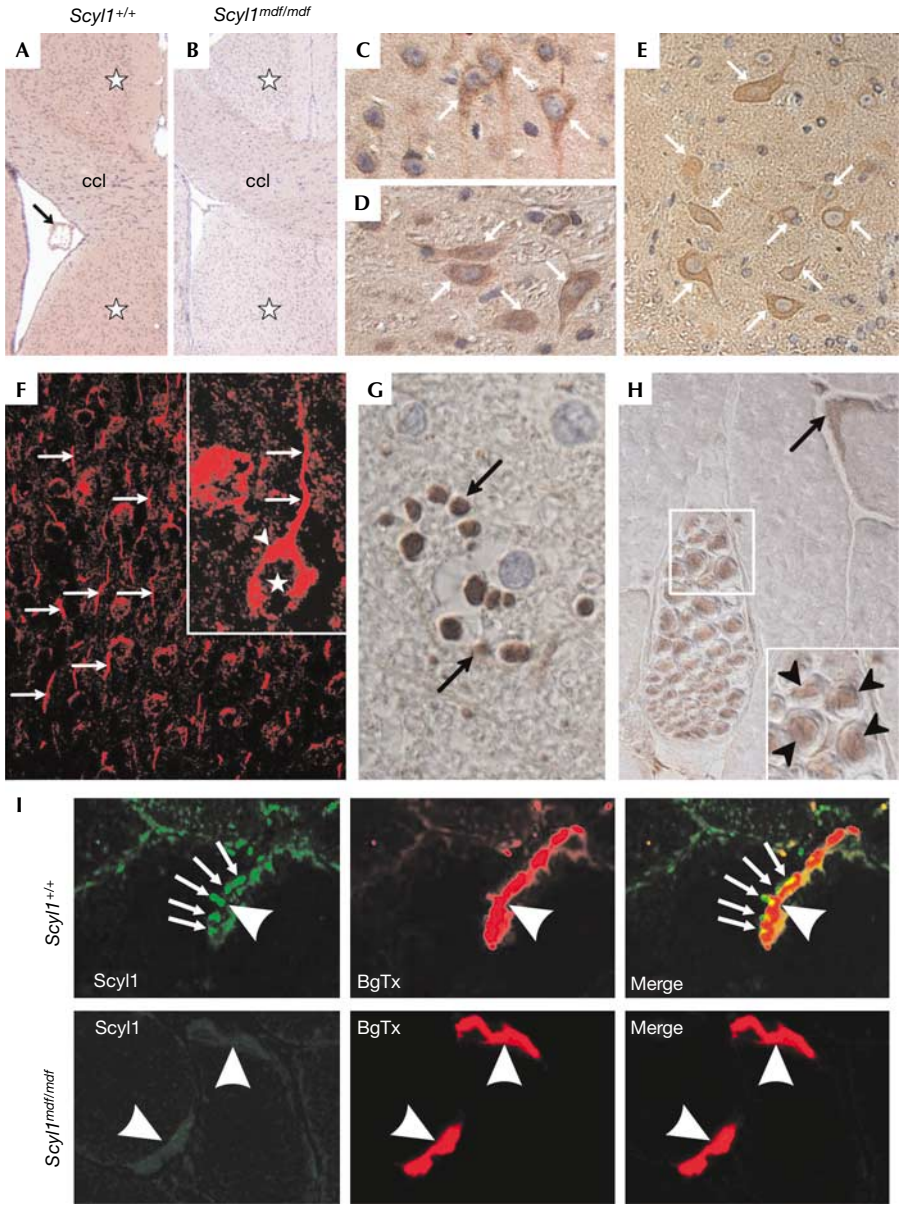

Fig 2 | Scyl1 protein is a neuronal protein expressed in the axoplasm and concentrated at synapses. (**A**,**B**) Immunodetection of Scyl1 on semicoronal brain sections from (**A**) wild type *Scyl1*$^{+/+}$, but a lack of reactivity in (**B**) *Scyl1*$^{mdf/mdf}$. Note the strong Scyl1-specific immunosignal of the neuropil (**A**, white stars) and of the choroid plexus (**A**, arrow) in wild type. The neuropil in mutant brain does not yield comparable immunosignals (**B**, white stars). ccl, corpus callosum. (**C**) Prominent Scyl1 staining of cortical neurons (arrows) and (**D**) brain-stem neurons (arrows) of wild-type mice. (**E**) Prominent Scyl1 reactivity of anterior horn motor neurons (arrows) in wild-type spinal cord. (**F**) Confocal immunofluorescence images showing intense Scyl1 staining in the cytoplasm (arrowheads) and axons (arrows) of murine cerebral cortex neurons (white star, nonreactive nucleus). (**G**) Section from aged human brain showing SCYL1-specific immunosignal accumulation within axonal spheroids (arrows). (**H**) Strong axoplasmic Scyl1-specific staining of an intramuscular nerve branch in wild-type skeletal muscle (skm; arrowheads in inset). Scyl1 reactivity of a neuromuscular junction (NMJ) is indicated (arrow). (**I**) Scyl1 distribution at a wild-type NMJ: pronounced labelling of presynaptic terminal axons (arrows) and weaker reactivity of the post-synaptic sarcoplasm (arrowhead). α-Bungarotoxin (BgTx, arrowhead) was used as a postsynaptic marker. Confocal overlay of Scyl1 immunosignals (green) with BgTx-specific red fluorescence shows predominant presynaptic Scyl1 expression, which was not detectable at NMJs in *Scyl1*$^{mdf/mdf}$ mice (lower panel). All immunostainings shown were performed using the antibody raised against the Scyl1 C terminus.

degeneration remains unclear. However, a very recently published study on the yeast orthologue Cex1p (Yor112wp), suggests a possible function in intracellular transport: Cex1p is a component of the nuclear aminoacylation-dependent transfer RNA export machinery and collects cargo from export receptors at the cytoplasmic side of the nuclear pore complex (McGuire & Mangroo, 2007). The idea of an evolutionarily conserved role of Scyl1 in nucleocytoplasmic transport

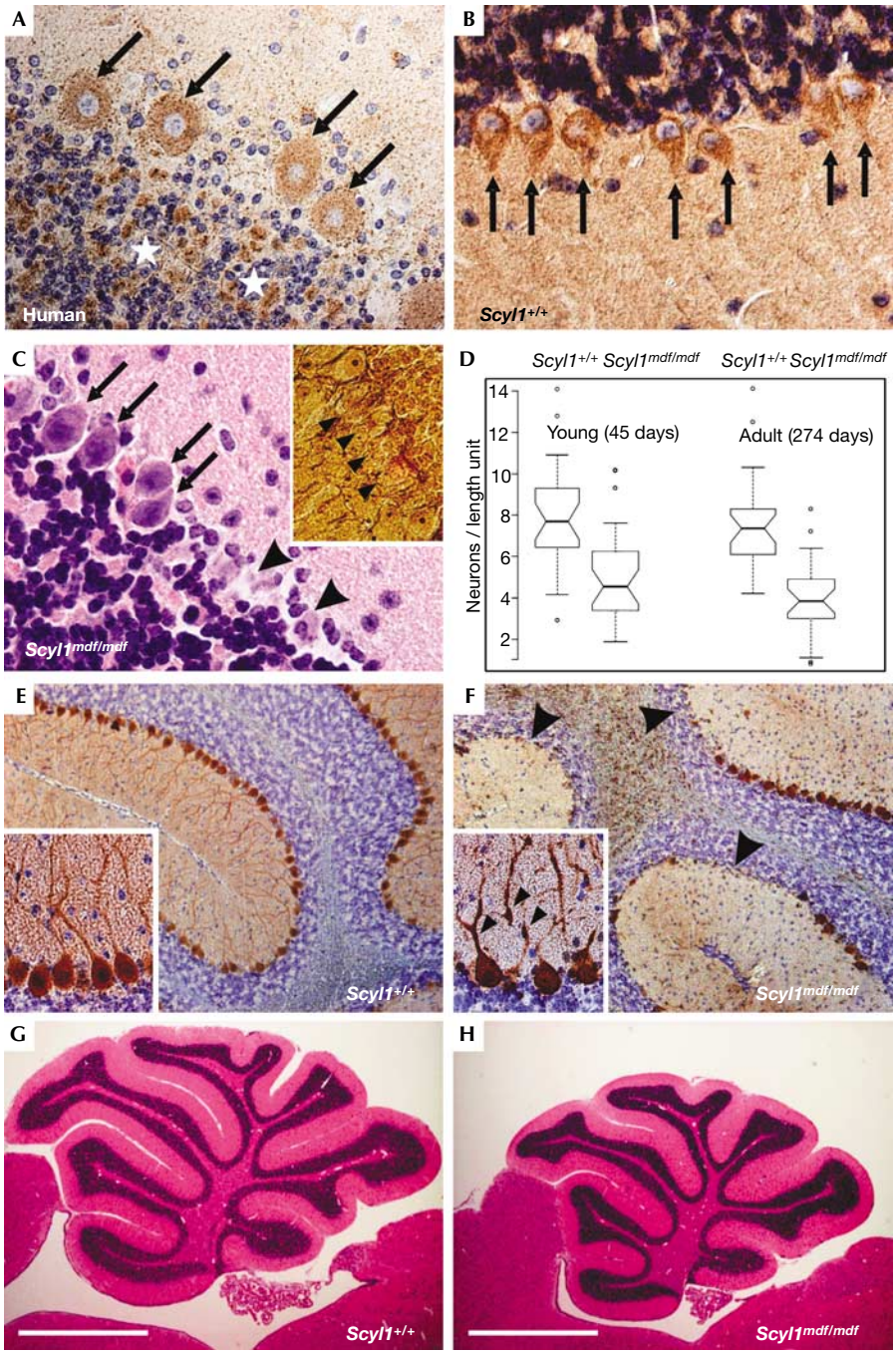

Fig 3 | Purkinje cell degeneration and cerebellar atrophy in *mdf*. (**A**) Immunodetection of SCYL1 in Purkinje cell (PC) somata (arrows) in human cerebellum with fine granular immunosignal accumulation in the synaptic region of the granular layer (white stars). (**B**) Scyl1-immunolocalization (carboxy-terminal antibody) in wild-type (*Scyl1*$^{+/+}$) mouse (255 days) cerebellum showing strong labelling within the PC layer. Arrows indicate the periodic continuity of PCs in wild-type cerebellum. (**C**) By contrast, PCs (arrows) in *Scyl1*$^{mdf/mdf}$-cerebellum (age-matched) were frequently abnormally shaped and displayed basophilic, condensed cytoplasm (H&E-staining). Arrowheads indicate discontinuity of the PC layer owing to the loss of single cells. Inset: two remaining PCs neighboured by persisting basket formations devoid of PCs (arrowheads), as shown by Bielschowsky staining. (**D**) Quantification of PC loss in *mdf*. PC counts in various areas of wild-type and *Scyl1*$^{mdf/mdf}$ cerebella show an overall loss of 42% in young mice ($P = 5.638e{-}05$, Kruskal-Wallis rank sum test) and 48% in adult mice ($P = 1.539e{-}07$), indicating early-onset and slowly progressive PC loss. Notches indicate confidence intervals of medians. (**E**) Immunostaining of calbindin D-28k in the cerebella of 274-day-old wild-type and (**F**) *Scyl1*$^{mdf/mdf}$ mice, showing pronounced loss of PCs (arrowheads). Insets: commensurate close-up views of representative PCs showing regular and complex dendritic arbors in wild-type-cerebella (inset in **E**), whereas multiple swellings (inset in **F**, arrowheads) and paucity of arborization are hallmarks in *mdf*. (**G**,**H**) H&E-stained median-sagittal sections of cerebella from (**G**) age-matched wild-type and (**H**) *Scyl1*$^{mdf/mdf}$ mice showing atrophy of *mdf* cerebellum compared with wild-type. Scale bars, 1 mm. H&E, haematoxylin and eosin.

is supported further by reported interactions with the nuclear pore protein NUP98 and the nuclear export receptor exportin-7 (XPO7). Therefore, we propose that Scyl1 defciency in neurons might cause degeneration owing to a defect in the nucleocytoplasmic transport machinery, a new pathway involved in neurodegeneration.

METHODS

Animals used in this study. We obtained *mdf* mice (B6C3Fe a/a-mdf/J) from the Jackson Laboratory (Bar Harbor, ME, USA), where *mdf* originally emerged as a spontaneous autosomal recessive mutant in a C57BL/6J-*In fz* stock (Womack *et al*, 1980). Mice stocks were maintained at the Division of Laboratory Animal Science and Genetics (Medical University Vienna, Himberg, Lower Austria) following institutionally approved protocols for the humane treatment of animals. Animals were killed by cervical dislocation.

Genetic mapping and high-throughput sequencing. We generated an intercross by breeding B6C3Fe-*mdf*-mice with *SJL* mice. Fine mapping was carried out by PCR for markers D19Mit32, D19Mit68, D19Mit59, D19Mit109 and D19Mit126. Corresponding PCR fragments were generated from 123 *mdf/mdf* mice (correlating to 246 meioses) by standard PCR, using fluorescence-labelled primers. PCR products were separated in an ABI3100 DNA sequencer (Applied Biosystems, Foster City, CA, USA) and subsequently analysed with the GenScan and Genotyper Software (Applied Biosystems).

Primers for all coding exons of the 48 candidate genes located in the critical interval were designed using Exon Locator and eXtractor (http://variation.swmed.edu/ex_lax/elxrdb_query.html), allowing amplification of all fragments under the same PCR conditions. PCR products were purified using 96-well filter plates (Millipore, Billerica, MA, USA) on a Miniprep robot (TECAN, Crailsheim, Germany). The fragments were sequenced using BigDye Version 3.1 (Applied Biosystems), according to the manufacturer's recommendations. Sequences were purified using the 96-well filter plates (Millipore), using the Miniprep robot and separated in an ABI3730 sequencer (Applied Biosystems). Sequence traces were then analysed using the SeqMan software (DNASTAR, Madison, WI, USA).

***Scyl1* genotyping.** After identification of the *Scyl1* mutation, the single-nucleotide insertion was genotyped by a PCR assay using allele-specific primers. After subjecting mouse tail-tip DNA to PCR amplification, the respective genotypes were deduced from banding patterns after electrophoretic separation of reaction products on polyacrylamide gels and visualization by fluorescence scanning (Typhoon; GE Healthcare, Chalfont St Giles, UK).

***In situ* hybridization.** Cryosections (10 μm) of wild-type mouse brains were probed for Scyl1-specific probes. A 475 bp complementary DNA reverse transcription–PCR (RT–PCR) product was generated with primers 5′-AGCCAGCTGAGAAGCAGAAG-3′, and 5′-ATAGGACCCTGGTCGTCCTT-3′, and subsequently inserted into the pCR II TOPO Vector (Invitrogen, Carlsbad, CA, USA). Templates for antisense and sense probes were generated by digesting the plasmid with *Apa*I and *Kpn*I, respectively. RNA probes were generated using the RNA labelling Kit (Roche Diagnostics, Mannheim, Germany), in the presence of digoxigenin (DIG)-labelled UTP. Slides were fixed, dehydrated, hybridized overnight at 37 °C, thoroughly washed, dehydrated and stained with DIG antibody (Roche) and NBT-BCIP (nitro-blue tetrazolium chloride and 5-bromo-4-chloro-3′-indolyphosphate p-toluidine salt).

Quantitative real-time PCR. Total RNA was extracted from muscle and brain tissue of *Scyl1*$^{+/+}$ and *Scyl1*$^{mdf/mdf}$ mice, respectively, and transcribed into cDNA by SuperScript II Reverse Transcriptase (Invitrogen) using random hexamer oligonucleotides. To quantify the amount of *Scyl1* mRNA, we used a real-time RT–PCR assay based on TaqMan technology, involving separate amplification of *Scyl1* and an internal reference, β-2-microglobulin (*B2m*), using commercial Taqman probes (Applied Biosystems; assays-on-demand: *Scyl1*–Mm00452459_m1; *B2m*–Mm00437762_m1). Quadruple measurement of each cDNA was calculated. The amount of *Scyl1* mRNA was calculated using the comparative C_t method ($\Delta\Delta C_t$) as described previously (Thiel *et al*, 2003).

Generation of polyclonal antibodies. Two polyclonal antibodies were directed against the unique mouse amino-acid sequences MWFFARDPVRDFPFEL or KGPMKLGARKLD, present either at the N terminus (aa 1–16, Scyl1-N) or at the C terminus (aa 795–806; Scyl1-C) of Scyl1. Peptides were synthesized with terminal cysteine residues, conjugated to the carrier protein keyhole limpet haemocyanin and purified by a commercial laboratory (Gramsch Laboratories, Schwabhausen, Germany). Antibodies from rabbit antisera were purified by affinity chromatography using the corresponding peptides coupled to thiopropyl sepharose 6B (GE Healthcare). Antibody specificity was established by pre-adsorption of the antibodies with their cognate peptide antigens, which completely abolished immunoreactivity (supplementary Fig 2B,C online). Owing to high homology, both antibodies recognize human SCYL1 and are predicted to crossreact with the rat homologue of Scyl1.

SDS–polyacrylamide gel electrophoresis and western blots. Tissue extracts were prepared by disruption in lysis buffer (120 mM Tris (pH 6.8), 200 mM dithiothreitol, 4% SDS, 20% glycerol) and separated on 6–12% polyacrylamide Tris–glycine SDS gels, and electrotransferred onto polyvinylidene difluoride or nitrocellulose membranes (Hybond, GE Healthcare). Equal loading of total protein was ascertained by electrophoresis of extracts on separate gels stained with Coomassie blue and densitometric analysis using the ImageJ software package. Detection was carried out with AP-conjugated secondary antibodies (1:1,000) and NBT-BCIP. Scyl1 antibodies were used at 1:800 dilution (Scyl1-C) or 1:200 (Scyl1-N).

Histology and immunohistochemistry. After dissection, tissues were snap-frozen in dry ice-cooled 2-methylbutane. Tissue samples were stored at −80 °C and cut on a cryostat. Cryosections were stained with haematoxylin and eosin (H&E). For paraffin-embedded histology, tissues were fixed in 3.7% paraformaldehyde, embedded in paraffin and subsequently processed for respective histological analyses.

Purkinje cell counts were taken by two independent, blinded investigators on the basis of H&E-stained cerebellar sections from age-matched wild-type and *mdf*-mutant mice. To account for variant Purkinje cell densities in different folia, a series of representative images were obtained ($n \geqslant 25$). Images were analysed using ImageJ and Purkinje cells were counted on segmented lines and adjusted to an arbitrary length unit. Statistical analysis using the Kruskal–Wallis rank sum test and boxplots were prepared with the statistical software package R (http://www.r-project.org).

Bielschowsky's silver impregnation method was carried out by treating formalin-fixed paraffin-embedded sections with silver nitrate, followed by reduction to visible metallic silver.

For immunohistochemistry, 10 μm cryosections were fixed using 3.7% paraformaldehyde (room temperature, 20 min), rinsed in PBS and subsequently incubated with polyclonal rabbit Scyl1-C-antibody (1:500) or goat Calbindin D-28K antibody (Sigma, St Louis, MI, USA). Secondary antibodies were conjugated to Alexa Fluor 488, Alexa Fluor 594 (Molecular Probes and Invitrogen, Eugene, OR, USA) or to horseradish peroxidase, respectively. Neuromuscular junctions were detected by α-Bungarotoxin conjugated with Alexa Fluor 594 (Molecular Probes). Immunostained sections were analysed using a confocal laser scanning microscope (Fluoview; Olympus, Tokyo).

Electron microscopy and morphometric analysis. Animals were transcardially perfused with 4% paraformaldehyde/1% cacodylate buffer and dissected brain tissue was fixed in cacodylate-buffered glutaraldehyde, embedded in epoxy resin and processed for transmission electron microscopy. Optic nerve images were analysed with ImageJ and myelin sheath thickness and g-ratios using outer and inner diameters were calculated from feret diameters.

Supplementary information is available at *EMBO reports* online (http://www.emboreports.org).

ACKNOWLEDGEMENTS

We thank R. Wegscheider, M. Hagl, D. Jovanovic and B. Dellinger for their excellent technical support, and I.B.H. Wilson for critically reading the manuscript. We thank G.E. Lienhard, Department of Biochemistry, Dartmouth Medical School, Hanover, NH, USA, for providing Scyl1-antiserum. This work was funded in part by the Austrian Society for Research on Neuromuscular Disorders and the Deutsche Forschungsgemeinschaft (KR 2334/1-1 and KR233/1-2).

REFERENCES

Blot S, Poirier C, Dreyfus PA (1995) The mouse mutation muscle deficient (mdf) is characterized by a progressive motoneuron disease. *J Neuropathol Exp Neurol* **54:** 812–825

Humbert S, Saudou F (2006) The ataxia-ome: connecting disease proteins of the cerebellum. *Cell* **125:** 645–647

Kato M, Yano K, Morotomi-Yano K, Saito H, Miki Y (2002) Identification and characterization of the human protein kinase-like gene NTKL: mitosis-specific centrosomal localization of an alternatively spliced isoform. *Genomics* **79:** 760–767

Lein ES *et al* (2007) Genome-wide atlas of gene expression in the adult mouse brain. *Nature* **445:** 168–176

Lim J *et al* (2006) A protein–protein interaction network for human inherited ataxias and disorders of Purkinje cell degeneration. *Cell* **125:** 801–814

Liu SC, Lane WS, Lienhard GE (2000) Cloning and preliminary characterization of a 105 kDa protein with an N-terminal kinase-like domain. *Biochim Biophys Acta* **1517:** 148–152

Macedo-Souza LI, Kok F, Santos S, Amorim SC, Starling A, Nishimura A, Lezirovitz K, Lino AM, Zatz M (2005) Spastic paraplegia, optic atrophy, and neuropathy is linked to chromosome 11q13. *Ann Neurol* **57:** 730–737

McGuire AT, Mangroo D (2007) Cex1p is a novel cytoplasmic component of the *Saccharomyces cerevisiae* nuclear tRNA export machinery. *EMBO J* **26:** 288–300

Poirier C, Blot S, Fernandes M, Carle GF, Stanescu V, Stanescu R, Guenet JL (1998) A high-resolution genetic map of mouse chromosome 19 encompassing the muscle-deficient osteochondrodystrophy (mdf-ocd) region. *Mamm Genome* **9:** 390–391

Sweet HO (1983) Muscle deficient (mdf). *Mouse News Lett* **68:** 72

Thiel CT, Kraus C, Rauch A, Ekici AB, Rautenstrauss B, Reis A (2003) A new quantitative PCR multiplex assay for rapid analysis of chromosome 17p11.2–12 duplications and deletions leading to HMSN/HNPP. *Eur J Hum Genet* **11:** 170–178

Womack JE, MacPike A, Meier H (1980) Muscle deficient, a new mutation in the mouse. *J Hered* **71:** 68–72